

# Radar Backscattering of Intertidal Mudflats Observed by Radarsat-1 SAR Images and Ground-Based Scatterometer Experiments

Hoonyol Lee, *Member, IEEE*, Heesam Chae, and Seong-Jun Cho

**Abstract**—This paper presents the variation of the radar backscattering of intertidal mudflats in the west coast of Korea observed by Radarsat-1 synthetic aperture radar (SAR) images and investigates the related factors by an indoor experiment and a field experiment using a ground-based C-band scatterometer. The 15 Radarsat-1 SAR images of the intertidal mudflat near Jebu Island used in this study were all taken at around 6:30 P.M., which is an ideal local time for evaluating the daytime evaporation effects during the 12.4-h tidal cycle. An *exposure time map* and an *evaporation time map* of mudflats at the time of each SAR acquisition are calculated based on the tidal records, a digital elevation map generated by the waterline extraction method, and the normalized daily evaporation index. The radar backscattering of the upper intertidal mudflat did not show a monotonic change with evaporation time but a complex pattern. An indoor experiment using a C-band scatterometer on drying mud revealed an M-shaped change (increase–decrease–increase–decrease) of radar backscattering due to various factors that affect dielectric constant and roughness such as the drainage of surface water (increase), evaporation (decrease), mud cracking (increase), and further evaporation (decrease). The variation of backscattering observed from SAR images agreed well with the initial three stages of the indoor experiment (increase–decrease–increase) but did not show the final stage of decrease from continuous evaporation. A field experiment on natural intertidal mudflats showed not only the pattern related to the initial drainage and evaporation but also speckles from biological activity.

**Index Terms**—Evaporation time map, exposure time map, mudflat, normalized evaporation index, radar backscattering, Radarsat-1, synthetic aperture radar (SAR), scatterometer.

## I. INTRODUCTION

**I**NTERTIDAL flats are among the most rapidly and dramatically changing land features due to the ebb and flood of tidal water. During the 12.4-h tidal cycle, intertidal flats are regularly exposed to air at low tide and submerged into water at high tide so that the surface undergoes substantial changes

Manuscript received April 27, 2010; revised July 5, 2010; accepted September 19, 2010. Date of publication November 22, 2010; date of current version April 22, 2011. This work was supported by the Ministry of Land, Transport and Maritime Affairs of the Korean Government under Grant 07KLSGC03 from the Cutting-edge Urban Development—Korean Land Spatialization Research Project.

H. Lee and H. Chae are with the Department of Geophysics, Kangwon National University, Chuncheon 200-701, Korea (e-mail: hoonyol@kangwon.ac.kr; chae2380@nate.com).

S.-J. Cho is with the Korea Institute of Geoscience and Mineral Resources, Daejeon 305-350, Korea (e-mail: mac@rock25t.kigam.re.kr).

Color versions of one or more of the figures in this paper are available online at <http://ieeexplore.ieee.org>.

Digital Object Identifier 10.1109/TGRS.2010.2084094

in structural and electrical properties. Satellite remote sensing has been widely used to investigate the physical properties and changes of intertidal flats [1]–[6]. Satellite synthetic aperture radar (SAR) is particularly useful due to the continuity of data acquisition regardless of weather or sunlight conditions and the uniqueness of interaction of target surface in the microwave region.

The radar backscattering coefficient of the intertidal mudflat observed by the satellite SAR is particularly sensitive to the changes in surface roughness and dielectric constant that are affected by several factors such as drainage, evaporation, mud cracking, and the activities of living creatures on the surface, all dramatically changing in time. During the ebb tide when the flats are exposed to air, the drainage of remnant surface water increases surface roughness. The drainage rate of the surface water is related to exposure time (the duration of mud exposed to air), soil porosity, and the density of drainage channels [7]. After the complete drainage of the surface water, surface roughness is stabilized and evaporation plays a major role in reducing interstitial soil moisture [8]. Evaporation rate depends on the duration of exposure time to air, sunlight, and wind and the degree of humidity. In case of mudflats, cracks are often found in the upper intertidal flats where the exposure time is long enough and the daily evaporation rate is strong. Biological activities such as the motion of surface creatures and their sediment reworking add other complex factors to increase the surface roughness and the randomness of radar backscattering [9].

Radar backscattering of agricultural or land-covering soil has been extensively studied by *in situ* measurements [10]–[18] and theoretical modeling [19]–[25] as a function of surface roughness, surface morphology, soil type, porosity, salinity, and moisture contents. However, few studies have detailed the effects of such complex changes in the intertidal flat to radar backscattering. Van der Wal *et al.* [26] investigated the intertidal flats in the Westerschelde in southwest Netherlands by using seven ERS-1/2 SAR images acquired at around 10:40 A.M. local time in descending orbit. However, they could not fully observe the dependence of radar backscattering on drainage or evaporation because the maximum exposure time of the flats under direct sunlight were not more than 4 h. On the contrary, the Radarsat-1 satellite is in a dawn–dusk orbit and the ascending orbit passes at 6:30 P.M. local time [27] where the maximum exposure time under the sunlight can be almost 12 h. Therefore, we expect that Radarsat-1 SAR images in

ascending orbit, used in this study, are more suitable to observe the daytime evaporation effect of intertidal flats than any other satellites that are not in the dawn–dusk orbit such as ERS-1/2, Envisat, JERS-1, or TerraSAR-X.

The total area of the intertidal flat in South Korea is about 2800 km<sup>2</sup>, which comprises 3% of the land surface of South Korea [28]. About 83% (2300 km<sup>2</sup>) of the intertidal flat is located in the western coasts while the remaining 17% (480 km<sup>2</sup>) is in southern coasts. The tidal range of up to 9 m and strong tidal current characterize the western coast of Korea as a typical *macrotidal* environment. Preservation and development of such intertidal flats have long been debated in Korean society with conflicting arguments between environmental values of natural flats and industrial uses by reclamation. There have been several previous studies on the Korean tidal flats based on satellite images [29]–[31] but few studies on the temporal variation of radar backscattering that occurs on natural mudflats due to complex changes of surface roughness and moisture content.

In this paper, we focus on an intertidal mudflat in the western coast of South Korea and analyze the variation of the radar backscattering coefficient by using a series of Radarsat-1 SAR images and the ground-based C-band scatterometer experiments—indoor and outdoor.

Following the description of the study area in Section II, Section III presents the analysis of the radar backscattering changes of mudflats observed by a series of SAR images from the Radarsat-1 satellite in ascending orbit and its comparison with exposure and evaporation times. Section IV reports the results of an indoor experiment on drying mud using a C-band scatterometer that details the complex variation of radar backscattering due to drainage, evaporation, and mud cracking. Section V provides a field experiment on the natural mudflat with the scatterometer, followed by the concluding remarks in Section VI.

## II. STUDY AREA

The study area is located in Kyeonggi Bay in the west coast of South Korea (Fig. 1). The area is encompassed by Jebu Island to the west, Songko-ri to the east, and Baekmi-ri to the southeast. Intertidal flats in this area are typical muddy flats commonly found in the western Korean coast. The average tidal range is 524 cm with an average low tide of 171 cm, an average high tide of 695 cm, and an average sea level of 450 cm [32]. Intertidal mudflats in the study area can be divided into three zones: lower, middle, and upper intertidal zones according to elevation, exposure time, and sedimentary conditions [28]. The lower intertidal zone is exposed to air only at low tide, and its sediment is mostly composed of fine sand. The middle intertidal zone is regularly exposed to air and submerged by average tides and is composed of mud and silt. The upper intertidal zone is covered by high tides and is composed of finer mud. We are particularly interested in the upper intertidal zone that reveals the maximum effects of drainage and long-term evaporation observed by Radarsat-1 SAR images and by the indoor and outdoor experiments using a ground-based C-band scatterometer, as shown in the following three sections.

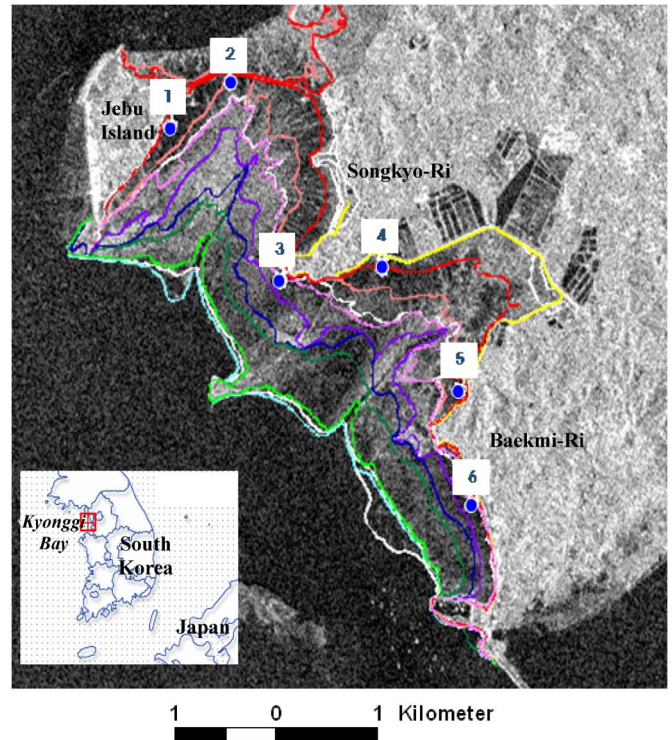


Fig. 1. Study area including the intertidal mudflat under investigation, surrounded by Jebu island, Songkyo-Ri, and Baekmi-Ri, in Kyonggi Bay in the western coast of South Korea. The regions from which the backscattering coefficients were extracted are shown from numbers 1 to 6. The waterlines extracted from 15 Radarsat-1 SAR images over the intertidal mudflat were shown over a Radarsat-1 SAR image taken at low tide on July 11, 2004.

## III. BACKSCATTERING OF MUDFLATS OBSERVED BY RADARSAT-1 SAR IMAGES

### A. Methods

A dedicated data processing strategy was used to compare the variation of the radar backscattering of the mudflats from Radarsat-1 SAR data with the *exposure time* and *evaporation time* of the mud (Fig. 2). We used 15 Radarsat-1 SAR images, with one obtained in 2001 and the others from 2003 to 2004. The images were all acquired at around 18:30 local time, which is an ideal time to observe the daytime evaporation effect on mudflats over a 12.4-h tidal cycle (Table I). All images were in S5 ascending mode with HH polarization at an incidence angle of 39° in the study area. The nominal resolutions were 15.7 m in slant range and 8.9 m in azimuth. Each SAR image was obtained in single-look complex data and averaged into four-look in the azimuth direction to reduce the speckles in the image. The images were then converted to the radar backscattering coefficient according to the gain parameters contained in the data header and then geocoded in the ground-range coordinates.

Fig. 3 shows the 15 Radarsat-1 SAR images of the study area in a complete tidal cycle from high tide, low tide, and back to high tide. The variation of waterlines, defined as the boundary between sea water and the mudflats exposed to air, is clearly visible and in accordance with the tidal sequence. However, the variation of radar backscattering on the mudflats does not simply follow the tidal sequence or exposure time, which will be analyzed in the following sections. The area of mudflats

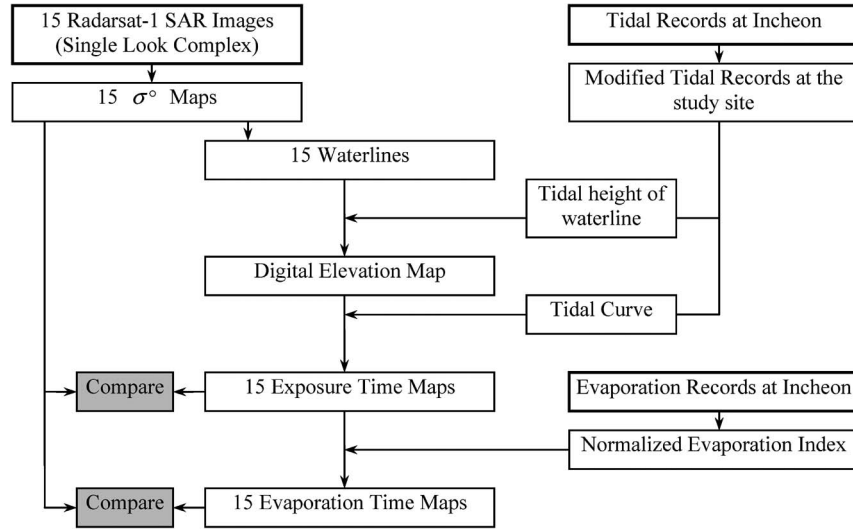


Fig. 2. Flowchart of Radarsat-1 SAR data processing for the comparisons of the backscattering coefficients of intertidal mudflats with the exposure and evaporation times.

TABLE I  
LIST OF RADARSAT-1 SAR IMAGES (ALL IN ASCENDING S5 MODE, 18:30 LOCAL TIME), TIDAL HEIGHTS, EVAPORATION LOSS, AND NORMALIZED EVAPORATION INDEX AT THE INCHEON TIDAL STATION LOCATED 30 km NORTH FROM THE STUDY SITE. THE TIDAL HEIGHTS WERE GEOGRAPHICALLY EXTRAPOLATED FROM THE INCHEON TIDAL DATA TO THE STUDY SITE

Scene No.	Acquisition Date (yyyy.mm.dd)	Tidal Height (cm, ebb/flood)	Evaporation Loss (mm)	Normalized Evaporation Index
1	2001.07.03	392, e	1.2	0.14
2	2003.05.06	648, f	1.0	0.12
3	2003.05.30	576, e	4.9	0.58
4	2003.06.23	288, f	1.5	0.18
5	2003.07.17	730, f	1.1	0.13
6	2003.08.10	406, e	1.1	0.13
7	2003.09.27	842, e	2.8	0.33
8	2003.10.21	266, f	0.9	0.11
9	2004.02.18	546, e	2.3	0.27
10	2004.07.11	263, e	0.9	0.11
11	2004.08.04	775, f	6.5	0.76
12	2004.08.28	461, e	3.0	0.35
13	2004.09.21	544, f	2.5	0.29
14	2004.10.15	820, e	2.8	0.33
15	2004.11.08	273, e	0.9	0.11

exposed to air and visible to as many images as possible is limited to the upper intertidal zone. To maximize the effect of exposure and evaporation times on radar backscattering, we selected six regions in the upper intertidal mudflats (Fig. 1) and extracted the backscattering coefficients by averaging over the 90 m × 90 m area for further analysis. The standard deviations of the backscattering coefficient within the area were typically 2–3 dB at six regions.

Accurate tidal records at the study site are essential to generate a digital elevation model (DEM), an exposure time map, and the exposure time map of the mudflats. As there is no tidal station at the study site, we modified the tidal records obtained from the Incheon tidal station located 30 km north from the study site. The tidal time ( $t_{study}$ ) and the tidal height ( $h_{study}$ ) of the study area can be calculated from the following [32]:

$$t_{study} = t_{ref} + \Delta t \tag{1}$$

$$h_{study} = (h_{ref} - \bar{h}_{ref}) \times \rho_{study} + \bar{h}_{study} \tag{2}$$

where  $t_{ref}$  is the tidal time of the reference station and  $\Delta t$  is the difference of the tidal time between the study area and the reference station (−10 min).  $h_{ref}$  is the tidal height record at the reference station, and  $\bar{h}_{ref}$  is the average sea level (464 cm) at the reference station.  $\rho_{study}$  is the tidal height rate between the study area and the reference station (0.96), and  $\bar{h}_{study}$  is the average sea level at the study area (450 cm). The modified tidal height at the time of each Radarsat-1 SAR acquisition is listed in Table I.

A DEM of the mudflat is necessary to calculate the exposure time but no such data exist with the accuracy necessary in this study. Similar to the method used in [29] and [30], we extracted waterlines from the 15 SAR images by visual inspection (Fig. 1) and designated the modified tidal height to each waterline. The waterlines with elevation were converted into a triangular irregular network DEM and then transferred to a DEM in raster format with a pixel size of 10 m × 10 m.

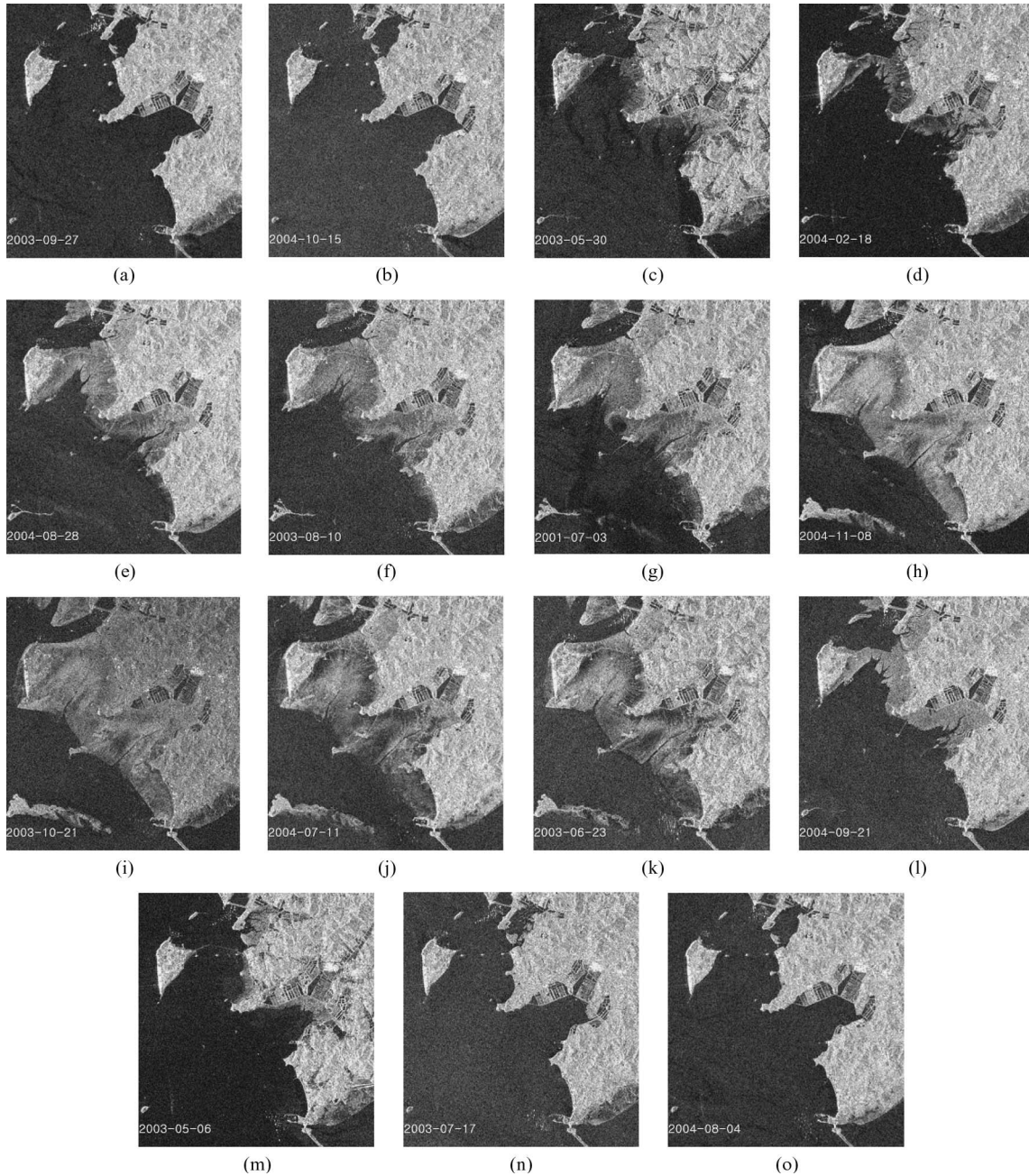


Fig. 3. Fifteen Radarsat-1 SAR images of the study area in tidal height sequence from (a) the highest tide to (j) the lowest during ebb current and then back to (k) the highest tide to (o) during flood current.

Using the DEM and the modified tidal records of the mudflats in the study area, the exposure time maps of the mudflats on each SAR image were generated. Fig. 4 shows an example of calculating the duration of exposition to air at a certain point with tidal height (or elevation) of 544 cm, for example, at the time of each SAR image acquisition at 18:30 local time on July 11, 2004. From the intersection between the modified tidal curve and the 544-cm tidal height, we can find that the point began to be exposed to air at 13:20 local time so that the exposure time is 5 h and 10 min on the point. The calculation is performed on each point of the mudflats on each SAR image to generate the exposure time maps. The

exposure time map on July 11, 2004 is shown in Fig. 5(a), as an example.

In addition to the exposure time, it is very likely that weather conditions such as temperature, humidity, solar radiation, and wind would affect the drainage and evaporation rate at the time of SAR image acquisition, but there was no *in situ* data available. Instead, we used the daily evaporation loss data measured at the Incheon weather station located about 20 km north from the study site. The daily evaporation loss is measured in millimeter scale by the difference of the level of water contained in an open cylindrical pan due to evaporation within a day [33]. The data were then normalized by dividing the value

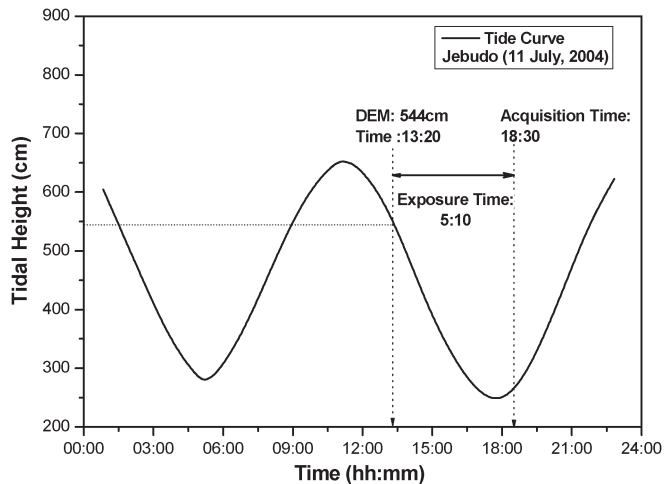


Fig. 4. Example of the calculation of the exposure time at a location having an elevation of 544 cm at the time of Radarsat-1 SAR acquisition on July 11, 2004. The exposure time can be calculated from the tide curve, elevation of the location, and the acquisition time of the Radarsat-1 SAR image.

by 8.5 mm, which is the maximum evaporation loss during the years 2001 and 2004, to give the *normalized evaporation index*. We then defined the *evaporation time* as follows:

$$[Evaporation\ Time] = [Exposure\ Time] \times [Normalized\ Evaporation\ Index]. \quad (3)$$

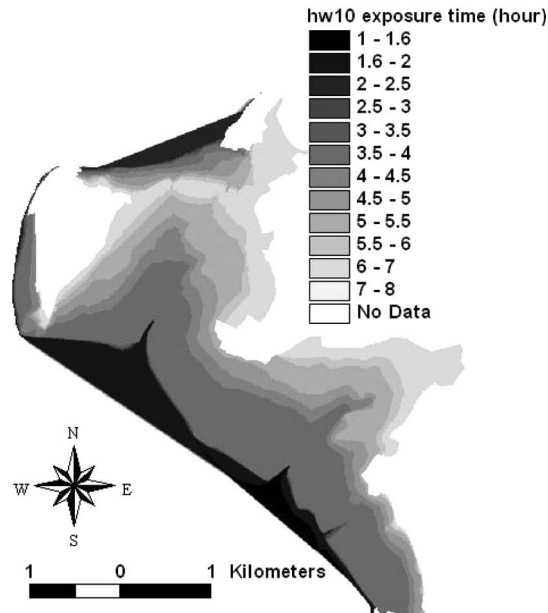
The evaporation time takes both the exposure time and the amount of evaporation loss of the mudflat into consideration and is more related to the drainage rate and the interstitial soil moisture of the mudflats than the exposure time alone.

**B. Results**

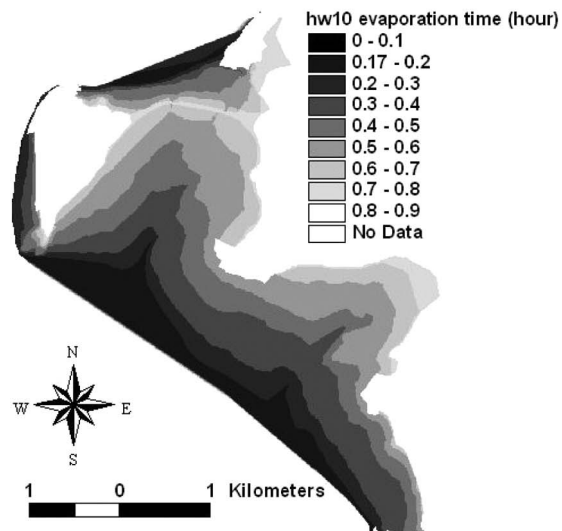
We compared the radar backscattering at six regions in the intertidal mudflat in the upper tidal zone (Fig. 1) with the exposure time as shown in Fig. 6(a). However, there is no particularly consistent trend between the six regions over the exposure time span up to 10 h. During the first 2 h, some regions (1, 4) showed a decrease and increase of backscattering while the others showed increase and decrease. Four regions (1, 2, 4, and 5) have exposure times longer than 5 h where the backscattering seems to rise, with the exception of region 4 where the backscattering drops significantly after 9 h. We concluded that the exposure time alone cannot reasonably explain the variation of backscattering from the natural mudflats.

Fig. 6(b) shows the relationship between the radar backscattering coefficient and the evaporation time. The graph shows a complicated trend rather than a monotonic decrease or increase of radar backscattering as the evaporation time increases but similar patterns are observed in all regions. At the early stage of evaporation time, the backscattering increased (AB), then decreased (BC), and increased again (CD).

To understand such complex variation of radar backscattering observed from a series of Radarsat-1 SAR images, we performed the following indoor and field experiments using a scatterometer system.



(a)



(b)

Fig. 5. Example of the (a) exposure time map and (b) evaporation time map of the mudflat at the time of Radarsat-1 SAR acquisition on July 11, 2004.

**IV. INDOOR SCATTEROMETER EXPERIMENT ON DRYING MUD**

**A. Methods**

To interpret the relationship of backscattering and the evaporation time of the mudflat, we performed a long-term laboratory experiment on drying mud using a scatterometer system. The scatterometer system is mainly composed of a vector network analyzer (Agilent 8753ES), a C-band antenna, a computer, a camera, RF cables, and a stand, as shown in Fig. 7(a). A horn antenna with a beamwidth of 15° was attached to the end of a 2-m stand with a fixed look angle of 45°. The center frequency was set to be 5.3 GHz with a bandwidth of 600 MHz and transmission power of 10 dBm. The scatterometer works in stepped-frequency sweeping mode, which obtains the data in frequency domain and converts the data into time domain via

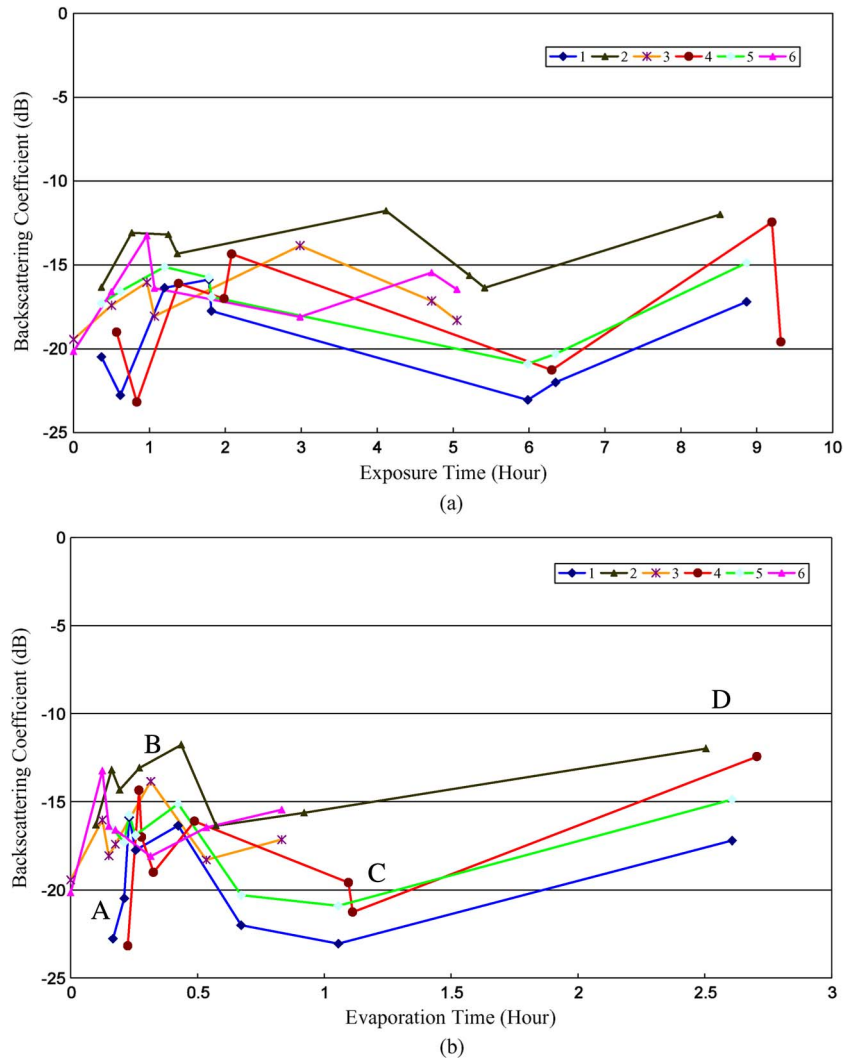


Fig. 6. Comparisons of radar backscattering coefficients with (a) exposure time and (b) evaporation time at the six regions in the upper intertidal mudflat. (a) shows no particular trend while (b) clearly shows the sequence of the increase (A–B), the decrease (B–C), and again, the increase (C–D) of radar backscattering coefficient with respect to evaporation time.

Fourier transform to give the range resolution of 25 cm in this case. The network analyzer was linked to a computer which controls the acquisition and archive of the data. A camera system was also linked to the computer to automatically take pictures regularly.

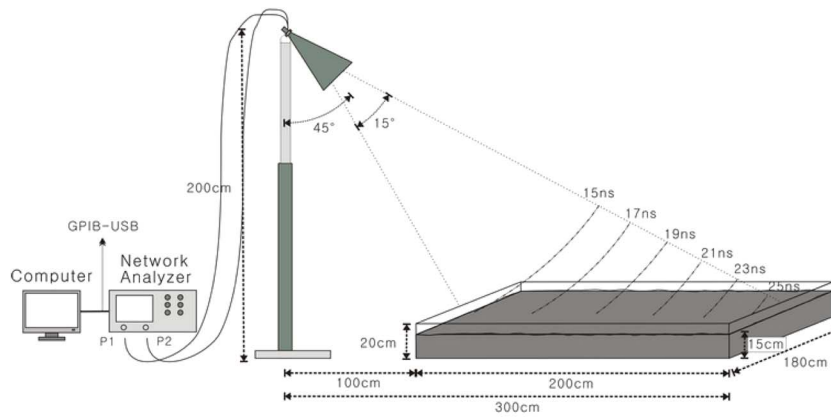
We brought 1200 kg of mud from the study area and put it into a 2-m-wide, 2-m-long, and 0.2-m-high Styrofoam frame, as shown in Fig. 7(b). Two-way travel times (and incidence angles) of microwave between the antenna and the mud sample were 15 ns ( $27^\circ$ ) at the front, 19 ns ( $45^\circ$ ) at the center, and 25 ns ( $56^\circ$ ) at the far range of the mud frame. The azimuth resolution at the center (19 ns) is 74 cm, which is less than half of the size of the frame. The mud sample was kept dry for six weeks from December 6, 2005 to January 21, 2006. The room temperature and humidity were initially set to  $20^\circ\text{C}$  and 30%, respectively, and controlled to be nearly constant. After January 5, 2006, the temperature was increased to  $28^\circ\text{C}$  and the humidity was lowered to 20% to speed up the evaporation. The radar backscattering of the drying mud sample was measured every 10 min, and photographs were taken every hour. We

measured gravimetric soil moisture from time to time. The gravimetric soil moisture was initially 60% and monotonically reduced to 15% on January 5, 2006 and then further reduced to 5% at the end of the experiment.

### B. Results

Fig. 8 shows the variation of radar backscattering from the mud sample measured at C-band and HH-polarization, which is the same as that of the Radarsat-1 SAR. The backscattering did not show a monotonic change because of the complicated change of surface roughness and dielectric constant over the entire drying sequence.

At the initial stage shown at point A in Figs. 8 and 9(a), the surface of mud was flooded with water and the backscattering was very low due to specular reflection. Surface water was then slowly drained out, increasing surface roughness, and the backscattering from the mud center (19 ns) increased accordingly, as shown in Fig. 8 (AB period) and, equivalently, in Fig. 9(a) and (b).



(a)



(b)

Fig. 7. (a) Schematic diagram and (b) photograph of the laboratory experiment on drying mud using a polarimetric scatterometer. The center of the mud sample is at 19 ns while the near side is at 15 ns and the far side is at 25 ns of the microwave two-way travel time.

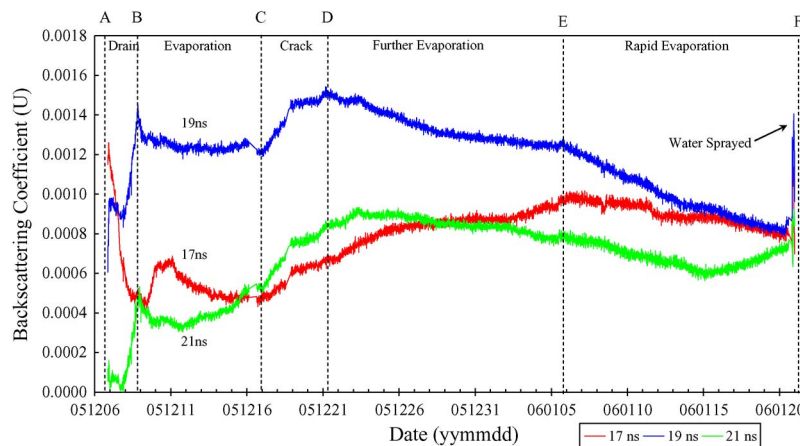


Fig. 8. Variation of radar backscattering coefficient (in decimal unit) obtained in the laboratory experiment using C-band and HH-polarization scatterometer. The center of the mud sample locates at 19 ns. An (A–E) M-shaped sequence came from the (A–B) rapid initial drainage of surface water followed by (B–C) evaporation, (C–D) crack development, (D–E) further evaporation, and (E to the end of the data) higher evaporation stage.

Meanwhile, there exist a period between A and B where the backscattering decreased for a short time. This was interpreted as a boundary effect of the laboratory experiment caused by the front part of the Styrofoam frame. Together with the smooth floor, the smooth and wet surface of the Styrofoam wall in the near range formed a dihedral corner reflector, resulting in strong

backscattering at 17 ns in the beginning of the experiment. During the AB period, the evaporation of water on the frame wall and the decrease of double bounce caused the rapid decrease of backscattering at 17 ns (near range) and also shortly obstructed the monotonic increase of backscattering at 19 ns (mud center) and 21 ns (far range).

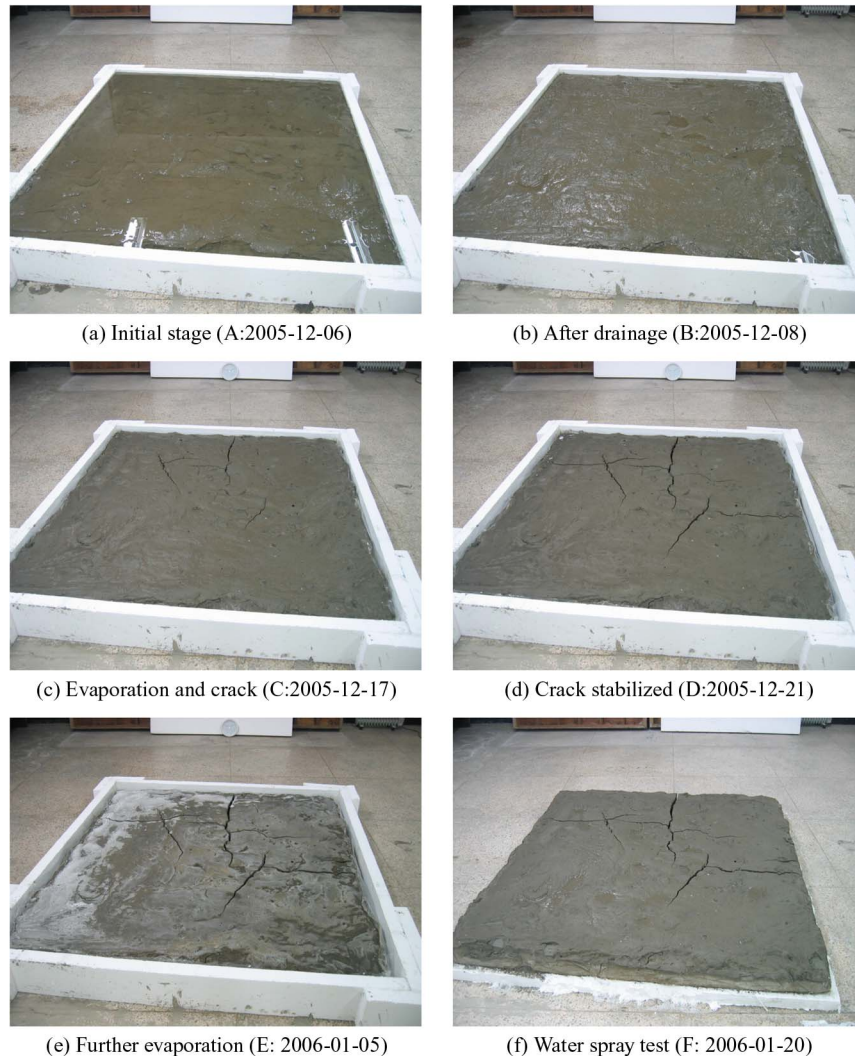


Fig. 9. Photographs of drying mud in the laboratory experiment pictured near the antenna position. (a) Initial flooded stage, (b) after drainage of surface water, (c) evaporation and crack development from the far range (21 ns), (d) fully developed cracks, (e) continuous drying, and (f) water spray test.

The backscattering stopped increasing when surface water was completely drained out (B) and began to decrease as the mud dried out, as shown in Fig. 8 (BC period) and Fig. 9(b) and (c). Volumetric contraction on the entire mud sample occurred during the BC period but the surface roughness remained the same. The decrease of backscattering during the BC period was due to the reduction of interstitial soil moisture caused by evaporation.

Near point C, mud cracks began to develop at the mud surface, rapidly increasing the surface roughness and, thus, backscattering in Fig. 8 (CD period) and Fig. 9(c) and (d). The development of mud crack started from the far range of the mud sample, which can be identified by the earlier rise of backscattering at the far range (21 ns) during the BC period than that of 19 ns. The backscattering of the mud center increased rapidly until the mud crack was fully developed and the surface structure was stabilized.

After point D, the mud sample was kept dry and the backscattering decreased monotonically due to the decrease of soil moisture, as shown in Fig. 8 (DE period) and Fig. 9(d) and (e). After point E, we increased the room temperature

to 28°C and lowered the humidity to 20% to accelerate the evaporation rate. As a result, the backscattering decreased more rapidly until the final stage of the experiment (point F).

On the final day of the indoor experiment, another experiment was performed, as shown at point F in Figs. 8 and 9(f). Water was gradually sprayed on the mud surface to increase the soil moisture but not to alter the surface structure from flooding of surface water. The backscattering was increased rapidly up to the cracking stage between C and D in Fig. 8. This was due to an increase of the dielectric constant of the surface while roughness remained constant. This spray test recursively confirmed the proportional relationship between the soil moisture and backscattering.

Consequently, the indoor scatterometer experiment has shown that the backscattering on drying mud has an M-shaped (*increase–decrease–increase–decrease*) variation: the initial *increase* from drainage of surface water (AB period), followed by the *decrease* from evaporation (BC period), *increase* due to mud cracking (CD period), and *decrease* due to continuous evaporation (DF period).

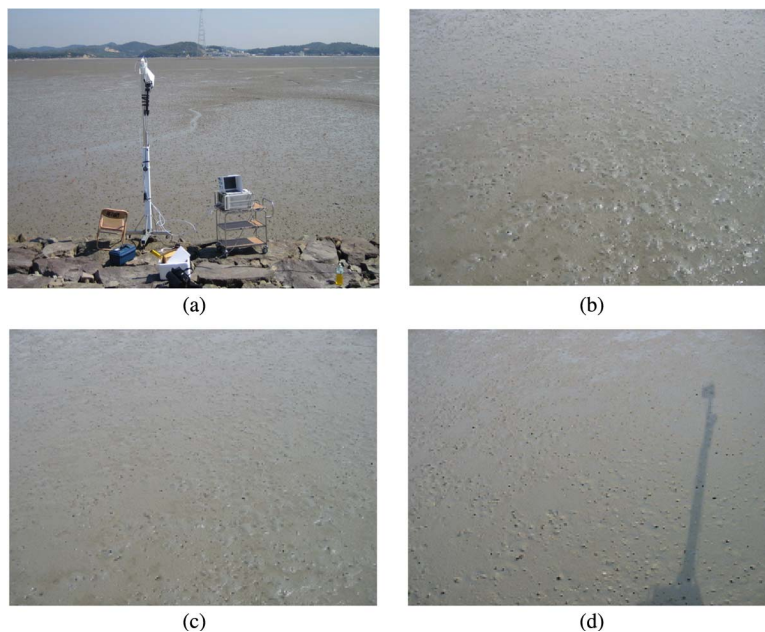


Fig. 10. Photographs taken from the field experiment on drying mudflat on May 10, 2006. (a) Field view of the experiment. Photographs of the mudflat taken at (b) 11:07, (c) 12:20, and (d) 17:10 local time.

From this indoor experiment, it was interpreted that the rapid increase of backscattering observed in the Radarsat-1 SAR images in the early evaporation time, shown as AB in Fig. 6(b), was due to the drainage of surface water, which is equivalent to AB in the indoor experiment in Fig. 8. The following decrease of backscattering in BC in Fig. 6(b) would be due to the evaporation similar to that of the indoor experiment, which is a common process in the natural mudflat. The possible reason of increase from C to D in Radarsat-1 SAR backscattering could be partially due to the mud cracking similar to that of the indoor experiment. During several field investigations to the study area, however, mud cracks were only found in a rare condition in the upper intertidal mudflat when the exposure time is longer than a tidal cycle during neap tide and the weather condition was extremely favorable to evaporation.

It is worth noting that the 15 images were taken over a two-year period and were acquired in different seasons. Both sediment conditions and surface roughness may change within the seasons due to different hydrodynamic conditions with more or less sedimentation of fine particles and biological activity. The indoor experiment performed in a confined environment may not fully explain the nature of mudflat. An advanced SAR system with higher temporal resolution could solve this multi-seasonal problem and thus investigate the effect of drainage, evaporation, cracking, or biological activities in a relatively short period. Therefore, we carried our scatterometer system and measured radar backscattering from natural mudflat, as presented in the following section.

## V. FIELD SCATTEROMETER EXPERIMENT

### A. Methods

The scatterometer system, identical to the one used in the indoor experiment, was installed on May 10, 2006 near region 2 in Fig. 1. The location and time were chosen to maxi-

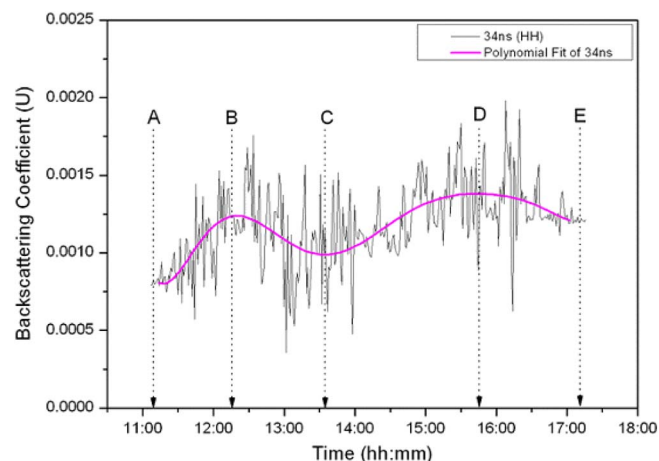


Fig. 11. Variation of backscattering coefficient on natural mudflat observed by the C-band HH scatterometer measurement on May 10, 2006.

mize the exposure time of the mudflat so as to see the effects of drainage and evaporation during the daytime. The height of the antenna was 5 m above the mudflat, and the incidence angle was fixed to  $45^\circ$ . Radar backscattering was measured every minute, and the photographs were also taken at the same interval [Fig. 10(a)].

### B. Results

Fig. 11 is the radar backscattering observed from 11:00 A.M. to 17:00. The signal was temporally very unstable due to the speckle effect of the targets. The major source of randomness was ocypodid crabs (*Macrophthalmus japonicus*) [9] of 3–5-cm size abundantly living in the mud. The system was left alone during the automatic measurements, and there was nobody within at least 100 m from the system. The photographs taken simultaneously with the scatterometer measurements confirmed

the rapid movements of crabs. The density of crabs fluctuated randomly from 60 to 100 per square meter. Crabs within the resolution cell of the coherent scatterometer system moved continuously and changed their body position, resulting in random variation of backscattering intensity, i.e., speckle. When we approached the test site to check the system, all crabs suddenly disappeared into their holes and the speckles disappeared. Such interventions occurred near A, B, and E in Fig. 11. The disappearance of crabs must have reduced the surface roughness to a local minimum in time but does not minimize the backscattering intensity. Backscattering intensities in such a calm situation have a local mean rather than a local minimum in time. This confirms that the speckle nature of biological activity is a stochastic process while backscattering from mud surface can be determined as shown in the door experiment. Therefore, the signal from the mudflat can be extracted by applying a moving-average filter to the original data. This procedure is equivalent to speckle filtering of SAR images.

The surface of the mudflat was initially inundated with water and slowly drained, showing the increase of backscattering from A to B in Fig. 11 and (b) to (c) in Fig. 10. Human intervention of the test site reduced the randomness of the signal from crabs. The surface was completely drained at point B in Fig. 11, and evaporation prevailed until the end of the experiment [E in Figs. 11 and 10(d)] but no mud cracking occurred. However, there was slight fluctuation of backscattering from C to D and then was reduced again from D to E even though mud crack was not developed during the experiments. The increase of backscattering from C to D could be due to the excavation of mud by the crabs from the holes. The digging of holes by crabs actually happened during the drainage but the effect to backscattering must have been weak until the surface was fully drained. The reduction of backscattering from D to E is hardy interpretable except the human intervention at the end of the experiment and, thus, the reduction of the speckle effect. However, the exact reason of the backscattering behavior from C to E is unclear from this experiment alone.

As a conclusion of the field experiment, we can observe the initial drainage and evaporation effect of mudflats in a relatively short period and can relate those phenomena to the indoor scatterometer experiment and satellite observations. We could also observed that the biological activity can play a major role in adding randomness of the signal and as well as surface roughness. Due to the short exposure time and evaporation rate during the field experiment, we could not fully evaluate the effect of cracks and long-term evaporation seen in the indoor experiment or from the Radarsat-1 SAR images.

## VI. CONCLUSION

The observation of 15 Radarsat-1 SAR images and the indoor and field experiments on mudflat have revealed that radar backscattering on intertidal mudflats has rather complicated behavior due to drainage, evaporation, mud cracking, and biological activity. The indoor scatterometer experiment on drying mud have shown a complete sequence of variation of backscattering that has an M-shaped (increase–decrease–increase–decrease) change due to drainage (increase), evaporation

(decrease), mud cracking (increase), and continuous further drying (decrease). A field scatterometer experiment on natural mudflats revealed not only the effect of initial drainage (increase) and evaporation (decrease) but also another important role of biological activities to radar backscattering in terms of structural change and speckle. From the comparison between radar backscattering observed by a series of Radarsat-1 SAR images and the evaporation time, which accommodates the exposure time and daily evaporation rate of the mud surface, we could observe the initial three stages (increase–decrease–increase) due to drainage, evaporation, and possibly from surface structural change by mud cracking and/or biological activity.

Due to different timescales of the three data sources—two years of the Radarsat-1 SAR images, two months of the indoor experiment, and one day of field work—and the difference of the temporal resolution of the data, we could not directly compare all the variations that might appear in the natural mudflat. It is expected that further accumulation of SAR data with higher temporal resolution would reveal the full-scale M-shaped variation on a drying natural mudflat. Field experiments on natural mudflats longer than a day—by placing the scatterometer system in a shelter—are necessary to see the effect of structural complexity given by mud cracking and prolonged evaporation to radar backscattering, which also remains as a future work.

Consequently, the results of this study imply that SAR image interpretation on intertidal mudflats should be carefully conducted, considering the various natural processes that might affect the radar backscattering. The key finding of this research was to identify the effect of drainage, evaporation, mud cracking, and biological activities to radar backscattering. Those environmental factors are all site and time dependent, which affect radar backscattering significantly. A huge amount of future works is open to the science community with advanced equipment and resources, including *in situ* measurements of environmental parameters and concurrent radar measurements to quantify the complex nature of intertidal flats.

## REFERENCES

- [1] M. G. Yates, A. R. Jones, S. McGrorty, and J. D. Goss-Custard, "The use of satellite imagery to determine the distribution of intertidal surface sediments of the Wash, England," *Estuarine Coast. Shelf Sci.*, vol. 36, no. 4, pp. 333–344, Apr. 1993.
- [2] A. G. Thomson, R. M. Fuller, T. H. Sparks, M. G. Yates, and J. Eastwood, "Ground and airborne radiometry over intertidal surfaces: Waveband selection for cover classification," *Int. J. Remote Sens.*, vol. 19, no. 6, pp. 1189–1205, Apr. 1998.
- [3] M. P. Rainey, A. N. Tyler, R. Bryant, D. J. Gilvear, and P. McDonald, "The influence of surface and interstitial moisture on the spectral characteristics of intertidal sediments: Implications for airborne image collection and processing," *Int. J. Remote Sens.*, vol. 21, no. 16, pp. 3025–3038, Nov. 2000.
- [4] M. P. Rainey, A. N. Tyler, D. J. Gilvear, R. G. Bryant, and P. McDonald, "Mapping intertidal estuarine sediment grain size distributions through airborne remote sensing," *Remote Sens. Environ.*, vol. 86, no. 4, pp. 480–490, Aug. 2003.
- [5] B. Deronde, P. Kempeneers, and R. M. Forster, "Imaging spectroscopy as a tool to study sediment characteristics on a tidal sandbank in the Westerschelde," *Estuarine Coast. Shelf Sci.*, vol. 69, no. 3/4, pp. 580–590, Sep. 2006.
- [6] D. van der Wal and P. M. J. Herman, "Regression-based synergy of optical, shortwave infrared and microwave remote sensing for monitoring the grain-size of intertidal sediments," *Remote Sens. Environ.*, vol. 111, no. 1, pp. 89–106, Nov. 2007.

- [7] C. R. Alexander, C. A. Nittrouer, D. J. Demaster, Y.-A. Park, and S.-C. Park, "Macrotidal mudflats of the southwestern Korean coast: A model for interpretation of intertidal deposits," *J. Sedimentary Petrology*, vol. 61, no. 5, pp. 805–824, Sep. 1991.
- [8] R. L. Folk, "A review of grain-size parameters," *Sedimentology*, vol. 6, no. 2, pp. 73–93, 1966.
- [9] Y. Henmi, "Life-history patterns in two forms of *Macrophthalmus japonicus* (Crustacea: Brachyura)," *Mar. Biol.*, vol. 101, no. 1, pp. 53–60, Jan. 1989.
- [10] N. R. Peplinski, F. T. Ulaby, and M. C. Dobson, "Dielectric properties of soils in the 0.3–1.3 GHz range," *IEEE Trans. Geosci. Remote Sens.*, vol. 33, no. 3, pp. 803–807, May 1995.
- [11] I. Champion and R. Faivre, "Sensitivity of the radar signal to soil moisture: Variation with incidence angle, frequency, and polarization," *IEEE Trans. Geosci. Remote Sens.*, vol. 35, no. 3, pp. 781–783, May 1997.
- [12] J. Sabburg, J. A. R. Ball, and N. H. Hancock, "Dielectric behavior of moist swelling clay soils at microwave frequencies," *IEEE Trans. Geosci. Remote Sens.*, vol. 35, no. 3, pp. 784–787, May 1997.
- [13] A. Quesney, S. Le Hégarat-Masclé, O. Taconet, D. Vidal-Madjar, J. P. Wigneron, C. Loumagne, and M. Normand, "Estimation of watershed soil moisture index from ERS/SAR data," *Remote Sens. Environ.*, vol. 72, no. 3, pp. 290–303, Jun. 2000.
- [14] M. Zribi, O. Taconet, and V. Ciarletti, "Effect of row structures on radar microwave measurements over soil surface," *Int. J. Remote Sens.*, vol. 23, no. 24, pp. 5211–5224, Dec. 2002.
- [15] P. C. Dubois, J. J. van Zyl, and T. Engman, "Measuring soil moisture with imaging radars," *IEEE Trans. Geosci. Remote Sens.*, vol. 33, no. 4, pp. 916–926, Jul. 1995.
- [16] J. Shi, J. Wang, A. Y. Hsu, P. E. O'Neill, and E. T. Engman, "Estimation of bare surface soil moisture and surface roughness parameters using L-band SAR image data," *IEEE Trans. Geosci. Remote Sens.*, vol. 35, no. 5, pp. 1254–1266, Sep. 1997.
- [17] Y. Oh, "Quantitative retrieval of soil moisture content and surface roughness from multipolarized radar observations of base soil surface," *IEEE Trans. Geosci. Remote Sens.*, vol. 42, no. 3, pp. 596–601, Mar. 2004.
- [18] Y. Lasne, P. Paillou, A. Freeman, T. Farr, K. C. McDonald, G. Ruffié, J.-M. Malézieux, B. Chapman, and F. Demontoux, "Effect of salinity on the dielectric properties of geological materials: Implication for soil moisture detection by means of radar remote sensing," *IEEE Trans. Geosci. Remote Sens.*, vol. 46, no. 6, pp. 1674–1688, Jun. 2008.
- [19] F. T. Ulaby, R. K. Moore, and A. K. Fung, *Microwave Remote Sensing Active and Passive, Volume II: Radar Remote Sensing and Surface Scattering and Emission Theory*. Norwood, MA: Artech House, 1981, pp. 827–833.
- [20] Y. Oh, K. Sarabandi, and F. T. Ulaby, "An empirical model and an inversion technique for radar scattering from bare soil surfaces," *IEEE Trans. Geosci. Remote Sens.*, vol. 30, no. 2, pp. 370–381, Mar. 1992.
- [21] R. M. Narayanan, R. Pardipuram, and D. C. Rundquist, "Statistical characteristics of simulated radar imagery from bare soil surfaces: Effects of surface roughness and soil moisture variability," *IEEE Trans. Geosci. Remote Sens.*, vol. 32, no. 1, pp. 159–168, Jan. 1994.
- [22] F. T. Ulaby and C. Elachi, *Radar Polarimetry for Geoscience Applications*. Norwood, MA: Artech House, 1990.
- [23] A. K. Fung, Z. Li, and K. S. Chen, "Backscattering from a randomly rough dielectric surface," *IEEE Trans. Geosci. Remote Sens.*, vol. 30, no. 2, pp. 356–369, Mar. 1992.
- [24] A. K. Fung and K. S. Chen, "An update on the IEM surface backscattering model," *IEEE Geosci. Remote Sens. Lett.*, vol. 1, no. 2, pp. 75–77, Apr. 2004.
- [25] J. R. Wang and T. J. Schmugge, "An empirical model for the complex dielectric permittivity of soils as a function of water content," *IEEE Trans. Geosci. Remote Sens.*, vol. GRS-18, no. 4, pp. 288–295, Oct. 1980.
- [26] D. Van Der Wal, P. M. J. Herman, and A. Wielemaker-van den Dool, "Characterisation of surface roughness and sediment texture of intertidal flats using ERS SAR imagery," *Remote Sens. Environ.*, vol. 98, pp. 96–109, Sep. 2005.
- [27] H. S. Srivastava, P. Patel, M. L. Manchanda, and S. Adiga, "Use of multi-incidence angle RADARSAT-1 SAR data to incorporate the effect of surface roughness in soil moisture estimation," *IEEE Trans. Geosci. Remote Sens.*, vol. 41, no. 7, pp. 1638–1640, Jul. 2003.
- [28] C. H. Ko, *The Korean Tidal Flat: Environment, Biology and Human*. Seoul, South Korea: Seoul Nat. Univ. Press, 2001, pp. 3–21.
- [29] J.-H. Ryu, J.-S. Won, and K. D. Min, "Waterline extraction from Landsat TM data in a tidal flat a case study in Gomsu Bay, Korea," *Remote Sens. Environ.*, vol. 83, no. 3, pp. 442–456, Dec. 2002.
- [30] D. Kim, W. M. Moon, S.-E. Park, J.-E. Kim, and H.-S. Lee, "Dependence of waterline mapping on radar frequency used for SAR images in intertidal areas," *IEEE Geosci. Remote Sens. Lett.*, vol. 4, no. 2, pp. 269–273, Apr. 2007.
- [31] S.-E. Park, W. M. Moon, and D.-J. Kim, "Estimation of surface roughness parameter in intertidal mudflat using airborne polarimetric SAR data," *IEEE Trans. Geosci. Remote Sens.*, vol. 47, no. 4, pp. 1022–1031, Apr. 2009.
- [32] Korea Hydrographic and Oceanographic Administration, *Tide Information*. [Online]. Available: [http://www.khoa.go.kr/info/tide\\_info\\_mean.asp](http://www.khoa.go.kr/info/tide_info_mean.asp)
- [33] Korea Meteorological Administration, *Observation Data Archive*. [Online]. Available: [http://www.kma.go.kr/weather/observation/past\\_tendays.jsp](http://www.kma.go.kr/weather/observation/past_tendays.jsp)

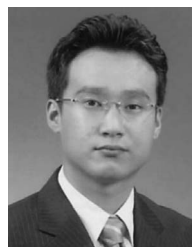


**Hoonyol Lee** (S'99–A'01–M'04) was born in Kwangju, Korea, in 1969. He received the B.S. degree in geology and the M.S. degree in geophysics from the Department of Geological Sciences, Seoul National University, Seoul, Korea, in 1995 and 1997, respectively, and the Ph.D. degree in radar remote sensing from the Department of Earth Sciences and Engineering, Imperial College London, University of London, London, U.K., in 2001.

From 2001 to 2003, he was a Postdoctoral Research Associate with Imperial College London.

From 2003 to 2004, he was a Senior Researcher with the Korea Institute of Geoscience and Mineral Resources, Daejeon, Korea. Since 2004, he has been with the Department of Geophysics, Kangwon National University, Chuncheon, Korea, where he is currently an Associate Professor. From August 2008 to July 2009, he was a Visiting Scholar with the Department of Geological Sciences, University of Oregon, Eugene. His research interests include synthetic aperture radar, interferometry, and polarimetry. He developed an educational synthetic aperture radar (eSAR) processor, a SAR Ocean Processor, polarimetric scatterometer systems, and ground-based SAR systems.

Dr. Lee was supported by the Korean Ministry of Education Scholarship, the Overseas Research Student Award from the Committee of Vice-Chancellor and Principals, U.K., and the Chevening Scholarship from the British Embassy in Korea for his Ph.D. study. He was awarded the Interactive Session Prize Paper Award at the 1999 IEEE International Geoscience and Remote Sensing Symposium, Hamburg, Germany. In 2008, he was the recipient of the Best Paper Award from the Korean Journal of Remote Sensing.



**Heesam Chae** was born in Wonju, Korea, in 1980. He received the B.S. and M.S. degrees in geophysics from Kangwon National University, Chuncheon, Korea, in 2005 and 2007, respectively.

From 2007 to 2009, he was a Researcher with the Korea Rural Community Corporation, Uiwang, Korea. His research interests include synthetic aperture radar and scatterometer systems and their applications to geophysical problems.



**Seong-Jun Cho** received the B.S. and M.S. degrees in mineral and petroleum engineering from Seoul National University, Seoul, Korea, in 1991 and 1993, respectively, and the Ph.D. degree in geophysics from the School of Urban, Civil and Geosystem Engineering, Seoul National University, in 2000.

Since 1996, he has been a Principal Geophysicist with the Korea Institute of Geoscience and Mineral Resources, Daejeon, Korea. From 2004 to 2005, he was with the Center for Northeast Asian Studies, Tohoku University, Sendai, Japan, as a Visiting researcher. His current interests include borehole radar and ground-penetrating radar imaging, low-frequency electromagnetic modeling and inversion, and geophysical measurement systems.